Adenosine Monophosphate as Shape-inducing Agent: The Case of Gold Nanostars

Carlos Fernández-Lodeiro,[a,b] Javier Fernández-Lodeiro,*[c,d] Adrián Fernández-Lodeiro,[c,d] Silvia Nuti,[c,d,] Carlos Lodeiro,[c,d], Alec P. LaGrow,[e] Ignacio Pérez-Juste,[b] Jorge Pérez-Juste*[a,b] and Isabel Pastoriza-Santos*[a,b]

[a] CINBIO, Universidade de Vigo, Campus Universitario As Lagoas, Marcosende, 36310 Vigo, Spain.

[b] Departamento de Química Física, Universidade de Vigo, Campus Universitario As Lagoas, Marcosende, 36310 Vigo, Spain.

[c] BIOSCOPE Group, LAQV@REQUIMTE, Chemistry Department, Faculty of Science and Technology, University NOVA of Lisbon, Caparica Campus, 2829-516 Caparica, Portugal

[d] PROTEOMASS Scientific Society, Rua dos Inventores, Madam Parque, Caparica Campus, 2829-516 Caparica, Portugal

[e] International Iberian Nanotechnology Laboratory, Braga, 4715-330, Portugal

Abstract

The seed-mediated growth of gold nanostructures is known to be strongly dependent on the gold seed nanocrystal structure but also in the presence of different additives that may influence the morphology, and therefore the crystalline structure of the final nanoparticle. Among the different additives or capping ligands, biomolecules are an interesting family due to their potential biomedical applications such as drug delivery, bioimaging, biosensing, phototherapy, and antimicrobial activities. Here, we develop a seed-mediated strategy for synthesizing uniform Au nanostars with tuneable optical properties that involves adenosine monophosphate (AMP) as capping ligand. The experimental data reveal the key role of AMP not just providing colloidal stability and directing the reduction of the gold precursor via complexation but also mediating the anisotropic growth of the Au seeds via its selective adsorption on the different crystalline facets of Au nanoparticles. These observations agree with theoretical simulations carried out using molecular dynamics and density functional theory (DFT) calculations. Interestingly, the obtained Au nanostars showed high thermal stability as well as colloidal stability in polar organic solvents, which allowed their direct silica coating via the Stöber method. Importantly, we also explored the mimic enzymatic activity of the resulting gold nanostars and observed a superior catalytic activity compared with the others gold nanoparticles reported in the literature.

KEYWORDS: Gold nanostars, AMP, shape-inducing agent, seed-growth method, nanozymes

Graphical Abstract

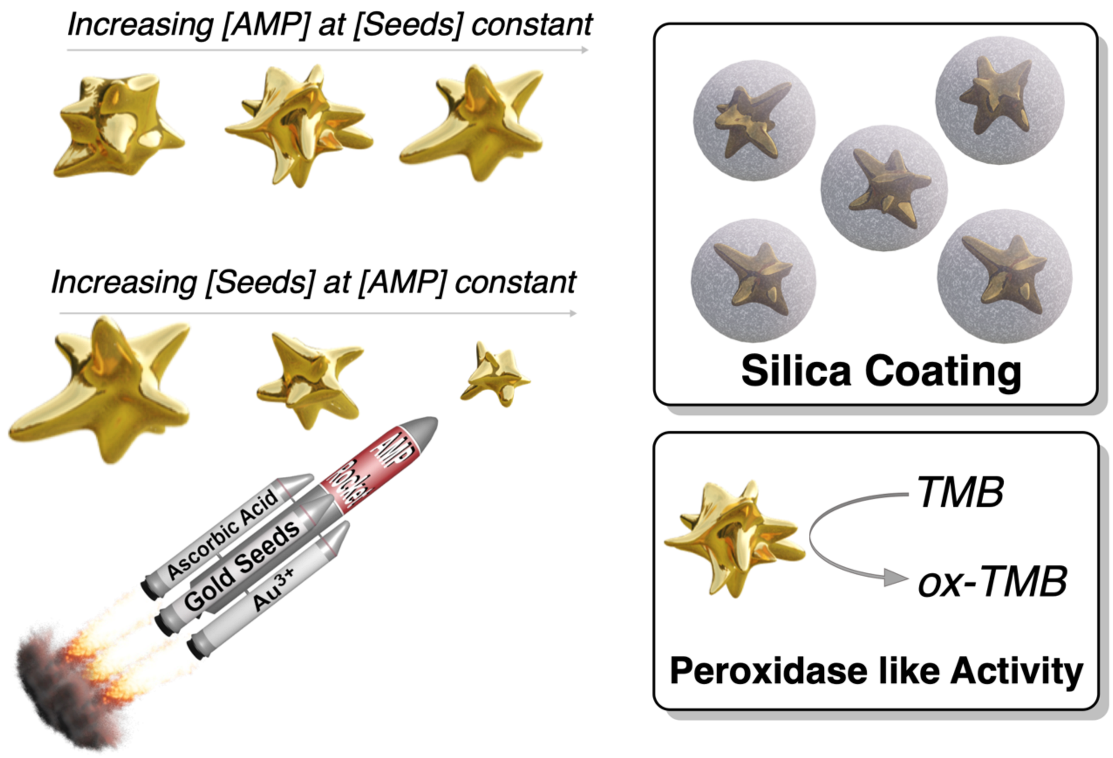

Introduction

The morphology of Au nanoparticles is strongly conditioned by the presence of capping ligands during the synthesis. In a seeded-growth mediated process, the capping ligands may interact with specific crystalline facets of the seed or even complex with the metal precursors. Therefore, apart from providing colloidal stability, they can strongly affect the reduction of the metal precursors or/and alter nanoparticle growth.[1]Among the large list of capping ligands, the biological molecules are rather appealing when we deal with biomedical applications such as drug delivery, bioimaging, biosensing, phototherapy, and antimicrobial activities. It has been already reported the use of different biomolecules, such as DNA, amino acids or peptides, as capping ligands to mediate the growth of Au nanoparticles. DNA can absorb or covalently bind to metal nanoparticles and direct their growth into different morphologies.[2],[3] Interestingly, chiral amino acids and peptides can induce the dissymmetric growth of Au nanoparticles to obtain chiral nanostructures with unique optical responses.[4],[5] Nevertheless, a lack of systematic study and understanding of the effect of a biomolecule on the NPs growth is often observed.[6]

Star-like gold nanoparticles (AuNSs) are perhaps the most studied anisotropic gold geometry at the nanometer scale after gold nanorods. Their tunable optical response in the visible-near infrared (Vis-NIR), dictated by the core size and number/ length of branches, and the strong light confinement at their tips[7] have fostered interest in these nanoparticles in a wide range of applications that include surface-enhanced spectroscopies,[8],[9] photonics,[10] cancer therapy[11] or (photo)catalysis.[12] A myriad of protocols based on colloidal chemistry has been developed to obtain AuNSs, with seeded growth approaches allowing for greater uniformity and better modulation of optical properties. In this regard, the features of the metal nanoparticles employed as seeds are one of the key factors to modulate the number of tips or overall dimensions of AuNSs without inducing noticeable changes in their optical response.[13] For example, smaller seeds lead to AuNSs with fewer tips deriving into more narrow optical properties in comparison with larger seeds.[13] Although multi-twinned seeds are most commonly used to promote the formation of nanostars, single crystalline seeds can also be employed by evolving them to NPs with twinned planes.

In the AuNS synthesis, polymers, surfactants, or discrete organic molecules were also reported as shape-directing agents. One of the first and widely used methods is based on the growth of tiny seeds using polyvinylpyrrolidone (PVP) as a reducing and capping agent and dimethylformamide (DMF) as a solvent.[13],[14] This strategy results in uniform nanostars with high yield and defined and tunable optical properties. Unfortunately, this method implies the use of DMF (toxic organic solvent) and PVP which may difficult the subsequent functionalization of the nanoparticles due to the lack of control of the PVP absorbed on the nanoparticle surface.[15] Water-soluble polymers, such as poly(allylamine hydrochloride) (PAH),[16] pyromellitic dianhydride-p-phenylene diamine (PPDDs),[17] or polystyrene sulfonate (PSS),[18] have been recently reported for the synthesis of AuNSs in water using seeded-mediated or seedless approaches, although in some cases the control in the optical properties is limited. Some surfactants can also direct the growth of AuNSs, such as quaternary ammonium surfactants,[19],[20] Triton X,[21] sodium dodecyl sulfate (SDS),[22] lauryl sulfobetaine (LSB)[23] or dioctyl sodium sulfosuccinate (AOT). For instance, it is hypothesized that cetyltrimethylammonium bromide (CTAB) preferentially adsorbs on the {100} gold seed facet, inducing the anisotropic growth via preferential deposition on the {111} face. However, surfactants are often highly cytotoxic or not environmentally friendly (especially in the case of CTAB or benzyldimethylhexadecylammonium chloride (BDAC)).

As an alternative to polymers or surfactants, discrete molecules such as hydroquinone (HQ), bis(p-sulfonatephenyl)phenylphosphine dihydrate dipotassium (BSPP) or the Good´s buffers family (e.g. EPPS, MOPS, HEPES) have been also employed for the synthesis of AuNSs.[24]–[28] The latter is probably the most commonly used for the seedless synthesis of AuNSs which importantly does not require additional surfactant, therefore, it is of interest due to its NPs biocompatibility and ease to functionalize. The limitations of this strategy are that requires tight control of different synthetic factors, the colloidal stability, or the presence of other Au NPs as subproducts with some Good´s buffers. Finally, biomolecules (albumin,[29] gelatin protein,[30] L-DOPA,[31] tryptophan-glutaraldehyde (Trp-GA)[32]) has been also employed for AuNSs synthesis although the reported results show broad plasmonic responses or limited plasmon tunning. **Table S1** summarizes different synthesis protocols of AuNSs and their main properties.

Therefore, the development of new synthetic strategies for AuNSs employing biomolecules that offer tuneability of plasmon response and with high colloidal stability remains a challenge. Nevertheless, it will facilitate the application of AuNSs in the medical arena. In this scenario, nucleotides are interesting capping ligands for the synthesis of metallic NPs[33]–[37] since are composed of a nitrogenous base that provides affinity for Au surface,[38] a five-carbon sugar (ribose or deoxyribose), and at least one phosphate group which provides colloid stability.[39] Adenosine monophosphate (AMP) is a nucleotide consisting of an adenine base linked to a ribose sugar with a phosphate group. Interestingly, it has been reported that adenine could bind to Au(III) species through the N7 site of purine ring forming Au(III)-AMP complexes. The high stability of such complexes has been ascribed to hydrogen bonding interactions and proton transfers.[40] In addition, AMP has been reported to adsorb on noble metal surfaces through either a ring nitrogen and/or the external NH_2 of the purine ring.[38] Both the complexation ability of the adenine moiety towards gold salt and the adsorption capabilities to metal surfaces makes AMP an interesting molecule with a dual role in AuNP synthesis. That is, AMP, as a complexing agent, can affect the reduction kinetics of the metal precursor and as a capping agent can provide colloidal stability and mediate the growth of Au nanoparticles.

Therefore, herein we investigated the use of AMP in the synthesis of AuNSs through a seed-mediated method. The role of AMP as a complexing and capping ligand was deeply analyzed and the experimental data was supported by computational studies employing molecular dynamics and density functional theory (DFT) calculations. Besides, the effect of other parameters such as concentration and size of Au seeds was studied. Next, we evaluated the behaviour of AuNSs in polar organic solvents and under heating (100°C) as well as the direct silica coating. Finally, the capabilities of the synthesized Au nanostars as peroxidase-mimicking nanozymes were studied employing as a model reaction the oxidation of the uncoloured 3,3′,5,5′-tetramethylbenzidine (TMB) into a blue oxidized TMB (ox-TMB) in the presence of H_2O_2.

Results and discussion

The complexation ability of the adenine moiety from AMP towards gold salt can strongly affect the formation kinetics of AuNPs. Therefore, we studied the influence of the complexation of AMP with the gold salt precursor ($AuCl_4^-$) on its redox properties. It is known that the addition of ascorbic acid to a $AuCl_4^-$ solution in the absence of any complexation agent leads to fast and uncontrollable nucleation and growth processes and the eventual nanoparticle aggregation due to the absence of stabilizing agents.[41] In the present case, the addition of ascorbic acid to an aqueous solution containing $AuCl_4^-$ and AMP at molar ratios of 1:2 or 1:4 just led to the partial reduction of $AuCl_4^-$ to $AuCl_2^-$, as indicated by the disappearance of the Au(III) CTT band located at ca. 305 nm (**Figure S1** in Supporting Information). This suggests that the complexation of $AuCl_4^-$ with AMP shifts its redox potential to more negative values. To give further insight into this experimental observation, different energy profiles for the binding mechanism of AMP to $AuCl_4^-$ were studied by means of DFT calculation (see details in Supporting information and **Figure S2**). **Figure 1** shows the most favourable energy profile suggesting that AMP interacts initially with the Au(III) salt to form a complex, $[AuCl_4\cdots AMP]^-$, mainly stabilized by a parallel interaction between the square planar $AuCl_4^-$ and the adenine unit in AMP. Upon reduction, the $[AuCl_4\cdots AMP]^-$ complex is transformed into $[AuCl_2\cdots AMP]^-$, which presents a strong direct interaction between the Au(I) atom and the N7 site in the adenine moiety. Interestingly, the additional reduction of $[AuCl_2\cdots AMP]^-$ complex to the final $[Au\cdots AMP]$ species is energetically unfavourable. This theoretical data predicted that additional Au seeds were needed to achieve the $[AuCl_2\cdots AMP]^-$ reduction to Au (0). Figures S3 and S4 in the SI show alternative complexation mechanisms predicting, in all cases, less favoured energy paths.

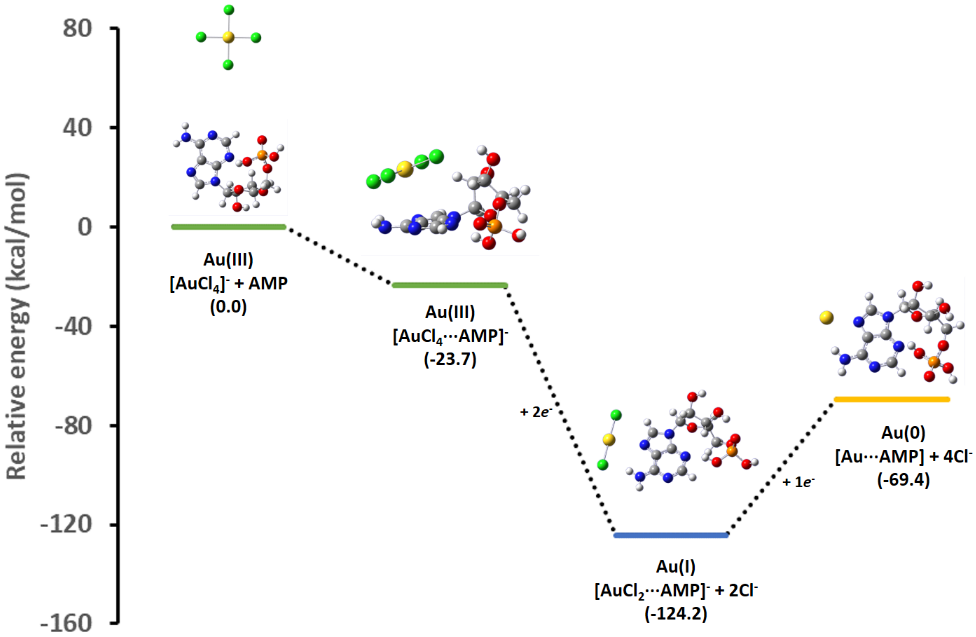

Figure 1. Theoretical relative energy profile for the interaction of $AuCl_4^-$ with AMP and its subsequent reduction intermediates.

To prove the autocatalytic process, tiny Au seeds stabilized by citrate were prepared using a strong reducing agent ($NaBH_4$). Firstly, the influence of the AMP concentration on the growth of Au seeds was studied while keeping constant the concentrations of gold salt (0.3 mM), ascorbic acid (0.3 mM) and Au seed (320 pM). **Figure 2** shows the influence of the AMP concentration on the optical properties as well as on the morphology of the overgrown Au nanoparticles. Thus, in the presence of 0.5 mM AMP (AMP:Au(0) molar ratio of 800), the resulting Au nanoparticles are characterized by a broad LSPR band located at *ca.* 650 nm with a shoulder at ca. 550 nm.[42] Besides TEM characterization revealed a star-shaped morphology with an overall size of 38.7 ± 5.0 nm and small tips of 5-10 nm in length (see **Figure 2B** and **Figure S5** in SI). With this information, we could assign the main LSPR to the tip localized plasmon mode and the shoulder at 550 nm to the core mode. Interestingly, the gradual increase in the AMP concentration from 0.5 mM to 0.9 mM led to a gradual red-shift of the main LSPR from 650 nm to 720 nm, 800 nm and 850 nm, corresponding to an increase in the AMP:Au(0) molar ratio from 960 to 1120, 1280 and 1440, respectively. The careful TEM analysis of the morphology of the Au nanostars (see **Figure 2** and **Figures S5** in SI) revealed that as the AMP:Au(0) molar ratio increased the number of tips per particle decreased but their length notably increased. Thus, Au nanostars synthesized at the highest AMP:Au(0) molar ratio (1440) presented tips with lengths up to 25-30 nm. Overall, the experimental results seem to indicate that the preferential adsorption of AMP on certain crystalline facets of Au seeds may be responsible for the anisotropic growth.

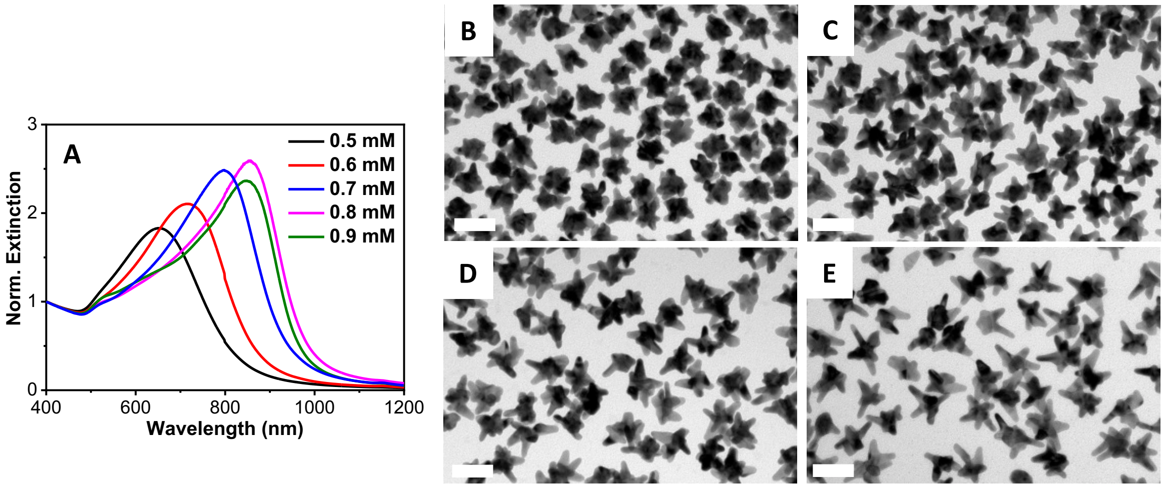

Figure 2. (A) Normalized extinction spectra of AuNSs obtained using different AMP concentration, as indicated. (B-E) Representative TEM images: (B) 0.5 mM AMP, (C) 0.6 mM AMP, (D) 0.7 mM AMP and (E) 0.8 mM AMP. $[Au]_{seed}$= 320 pM, $[AuCl_4^-]$=0.3 mM and [AA]=0.5 mM, kept constant in all cases. The scale bars represent 50 nm.

Next, the influence of Au seed concentration was explored while keeping the AMP concentration at 0.8 mM. **Figure 3A** shows the optical properties of the resulting Au nanostars upon decreasing the concentration of Au seeds from 1264 pM to 632 pM, 474 pM, 316 pM and 158 pM, corresponding to an increase in the AMP:Au(0) molar ratio from 320 to 640, 853, 1280 and 2560, respectively. It should be noted that the LSPR band red-shifted with decreasing the seed concentration from *ca.* 680 nm ($[Au]_{seed}$ = 1264 pM) up to *ca.* 950 nm ($[Au]_{seed}$ 158 pM). TEM characterization revealed that the red-shift is associated with; *i)* an increase of the overall dimension of the nanostars from 29.7±8.4 nm to 64.4±4.1 nm and *ii)* an increase in the average length of the spikes (see **Figure 3B-F** and **Figure S6** in SI). These observations agree with the previously reported data.[13],[16] Besides, an increase in the number of spikes per particle was also observed.

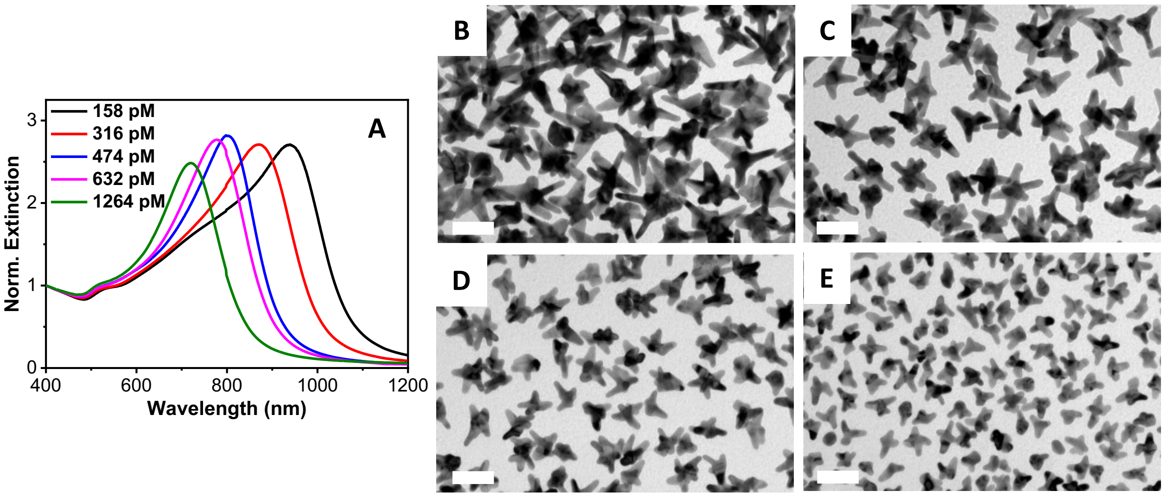

Figure 3. (A) Normalized extinction spectra of different AuNSs using different concentrations of Au seeds, as indicated. (B-E) Corresponding TEM images: (B) 158 pM, (C) 316 pM, (D) 632 pM and (E) 1264 pM (E) Au seeds concentration. [AuCl$_4^-$]=0.3 mM, [AA]=0.5 mM and [AMP]=0.8 mM, kept constant in all cases. The scale bars represent 50 nm.

To perform a more comprehensive study of the growth mechanism, time-resolved analysis of the synthesis of AuNSs was carried out by Vis-NIR spectroscopy and TEM. As can be seen in **Figure 4A**, at the initial stages (30 minutes) the nanoparticles present the main LSPR located at ca 730 nm that gradually red-shifts with time until reaching a constant value at *ca.* 880 nm. The TEM characterization of the particles at different stages, **Figure 4B-D**, showed that the tips/spikes are formed at the early stages of the reaction (30 minutes), and they grow in length throughout the reaction, being responsible for the observed red-shift in the LSPR.[42]

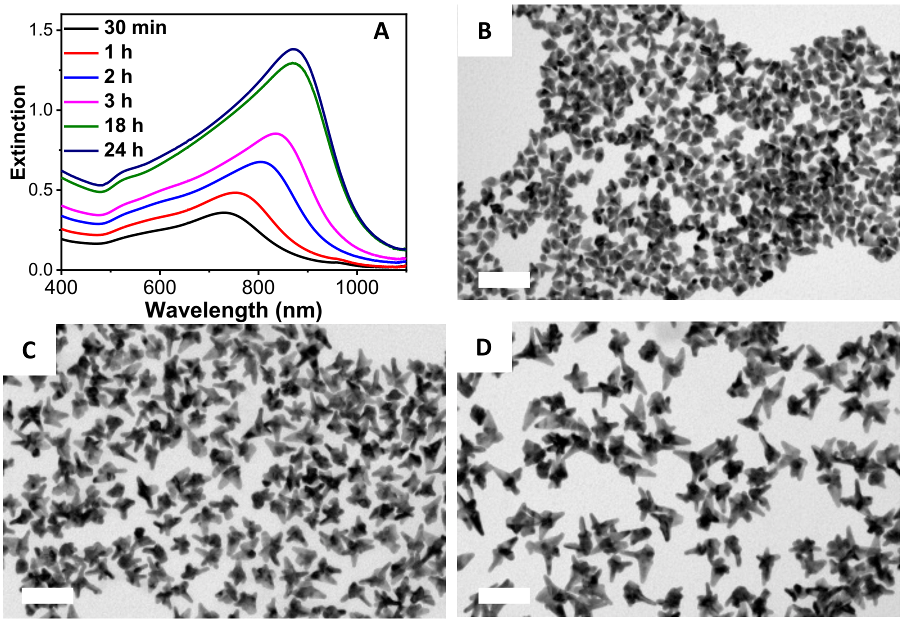

Figure 4. (A) Time evolution extinction spectra recorded during the formation of AuNSs. (B-D) TEM images of nanoparticles after (B) 30 minutes, (C) 3 hours and (D) 24 hours of reaction. [Au]$_{seed}$= 316 pM, [AuCl$_4^-$]= 0.3 mM, [AA]= 0.5 mM and [AMP]= 0.8 mM. Scale bars represent 100 nm.

The crystalline structure and morphology of AuNSs were carefully investigated by aberration-corrected high-resolution TEM (HRTEM) and High-angle annular dark-field scanning transmission electron microscopy (HAADF-STEM). **Figure 5** and **Figure S7** in SI show representative HRTEM analysis of two different AuNSs synthesized using the same concentration of Au seeds (320 pM) but different AMP concentrations (0.8 mM and 0.6 mM). As it is shown in **Figure 5A-C**, most of the spikes present crystalline planes (111) and (200) and seem to grow perpendicular to the (111) direction where the defects are located and grow along the defect planes with a <211> preferential direction. Furthermore, most of the tips usually showed a twinning plane running down the branch to the core of the particle, which is evident in the tilted HAADF images at a range of angles depending on the arm (**Figure 5G-H**). Interestingly, variations in the AMP concentration did not give rise to changes in the crystalline structure of the AuNSs and just affected their morphology. **Figure 5I** and **Figure S7I** in SI show a 3D tomographic reconstruction of AuNSs obtained with 0.8 mM and 0.6 mM of AMP respectively where it is demonstrated the larger tips for AuNSs obtained with 0.8 mM AMP. Interestingly, and regardless of the AMP concentration, HRTEM images showed that the centre of the gold nanostars exhibited a multi-twinned structure resembling that of an icosahedron (**Figure S8** in SI).

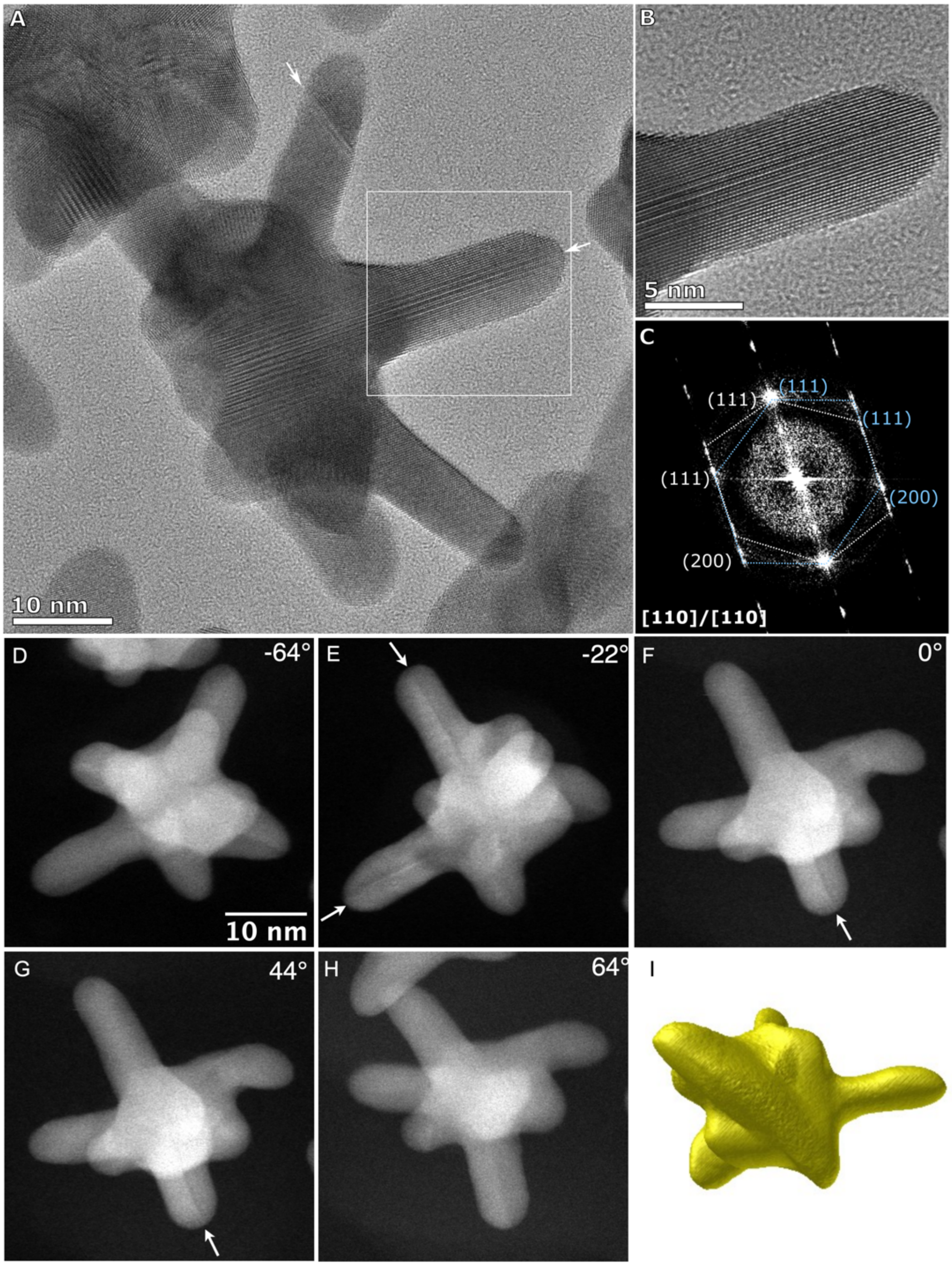

Figure 5. (A) Aberration corrected HRTEM of a gold nanostar synthesized using 0.8 mM AMP and 320 pM of Au seeds, the white arrows point towards twins in the tips. (B) Zoomed image of the tip from the white box in (A). A defect plane running down the centre of the tip is observed. (C) The FFT of (B) shows two zone axes both viewed down the [110] axis twinned along the (111) spacing. (D-H) HAADF-STEM images taken from the tomography tilt series. White arrows indicate when the defect plane extends along the tips. (I) 3D tomographic reconstruction of the nanostar.

Importantly, this AMP-mediated synthesis of gold nanostars may be also extended to larger Au seeds. As a proof of concept, citrate-stabilized spherical Au NPs with a mean diameter of *ca.* 30 nm were employed as seeds (see the experimental section for details). **Figure 6** shows the optical properties together with representative TEM images of the Au seed and the nanostars obtained upon increasing the AMP concentration from 0.4 mM to 0.9 mM (AMP:Au(0) molar ratios of 10 to 17.5 and 22.9) while keeping constant the Au seed concentration ($[Au]_{seed}$= 480 pM). As for the smaller Au seeds (see **Figure 2**), the increase in AMP concentration gave rise to a red-shift and a broadening of the main LSPR. It is in agreement with TEM results. Thus, TEM analysis revealed that the overall diameter ranged between 70-90 nm regardless of the AMP concentration, (**Figure S9** in SI). In addition, the mean length of the spikes increased from 5-10 nm for 0.4 mM AMP up to 30 nm in the presence of 0.9 mM AMP. On the other hand, the broadening in the optical response (see **Figure 3A**) could be ascribed to a larger core size and an increase in the number of spikes per particle. The morphological features and the optical response are in line with those previously reported PVP-stabilized AuNSs.[43]

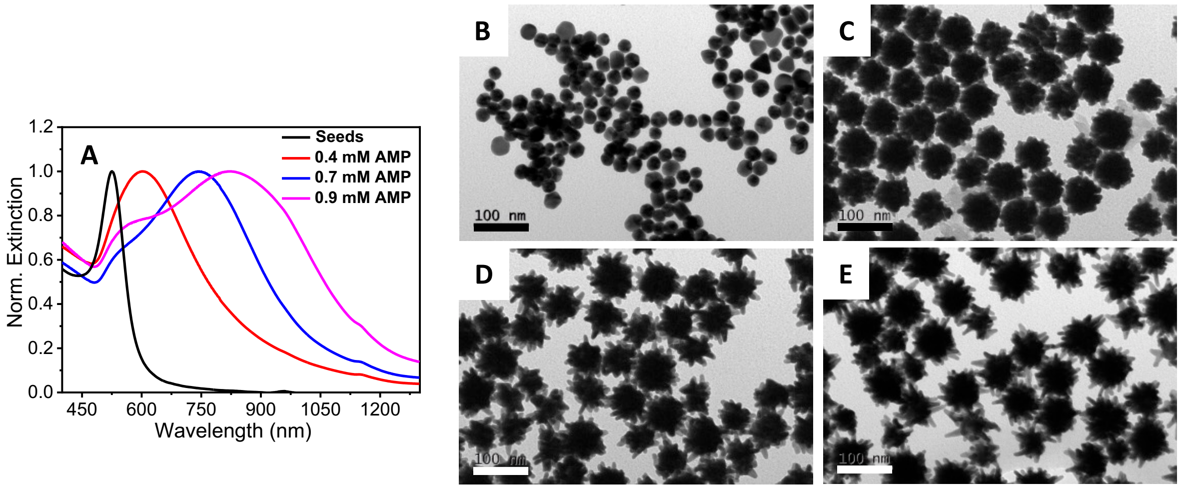

Figure 6. (A) Normalized extinction spectra of Au seeds and AuNSs obtained using different AMP concentrations. (B) TEM image of 30 nm citrate-stabilized Au seeds. (C-E) TEM images of AuNSs obtained using different AMP concentrations: (C) 0.4 mM, (D) 0.7 mM and (E) 0.9 mM. $[Au]_{seed}$= 480 pM, $[AuCl_4^-]$= 0.3 mM, [AA]=0.5 mM.

In order to propose a plausible mechanism for the synthesis of Au nanostars we have to take into consideration the following; ***i)*** the higher stability of the $[AuCl_2\cdots AMP]^-$ complex in comparison with the $[AuCl_4\cdots AMP]^-$ and $[Au\cdots AMP]$ complexes, as demonstrated by DFT calculation (Figure 1), ***ii)*** both types of citrate-stabilized Au seeds present multiple-twinned crystalline structure,[16] ***iii)*** the presence of twinning planes running along most of the tips (**Figure 5**) and, ***iv)*** the increase in length of the tips upon increasing the AMP concentration (**Figure 2**). Therefore, the experimental data demonstrates that AMP plays a fundamental role in the morphological transformation from the spherical shape of the seed to the star-shape of the overgrown particles. Such morphological transformation may be initially ascribed to the preferential adsorption of the AMP molecules towards certain crystal facets stabilizing them and promoting the deposition of gold adatoms towards less stabilized facets leading to the formation of tips/spikes through the Stranski–Krastanov growth mode.

Molecular dynamics calculations were employed to study the adsorption of AMP on different gold surfaces. To this purpose, we built up three model slabs for the Au{111}, Au{110} and Au{100} facets and the adsorption energy for a single AMP molecule on each slab was evaluated as previously proposed by Heinz[44] (see the Computational methods in Experimental section).

$$E_{\mathrm{ads}} = E_{(\mathrm{Au\{slab\}+AMP+H_2O})} - E_{(\mathrm{AMP+H_2O})} + E_{(\mathrm{H_2O})} - E_{(\mathrm{Au\{slab\}+H_2O})} \quad (1)$$

According to the results obtained, adsorption of AMP on the Au{111} surface (E_{ads} = -137.1 kcal/mol) was energetically more favourable than on Au{100} and Au{110} surfaces (E_{ads} = -103.9 kcal/mol and E_{ads} = -97.6 kcal/mol, respectively). A representative configuration for the adsorption of AMP on the Au{111} surface is depicted in **Figure 7A**, where it can be seen that AMP adopts a rather elongated disposition with the adenine moiety almost parallel to the metal surface (the average angle between the adenine plane and the top atomic layer of the gold slab is 6.3°). This disposition tends to maximize the number of contacts between the gold and nitrogen atoms in the adenine ring. Besides, the oxygen atom of the ribose ring is directed toward the surface at an average distance of 2.7 Å and the two OH bonds of the phosphate ring are also in close interaction with the metal. Interestingly, due to adsorption, there is a considerable reduction of the AMP conformational flexibility compared to its behaviour in an aqueous solution (see detailed description in **Figure S10-S12** in the SI). In particular, the adenine ring in isolated AMP adopts *syn* and *anti*-orientations with respect to the ribose unit due to rotation around the central C-N bond between both rings. However, this rotation is hindered due to adsorption and the adenine and ribose units are always *syn*-oriented (**Figure 7)**.

AMP also adopts extended or stretched configurations when adsorbed on Au{100} and Au{110} surfaces (see **Figure 7B and 7C**). However, the average angles between the adenine ring and the metal surface are slightly larger than for Au{111} (8.6° and 11.0° for {100} and {110}, respectively), and the average distances from the ribose oxygen atom to the first metal layer are also larger (2.8 Å and 3.8 Å, respectively, see Figure S13). These trends correlate with the smaller preference for adsorption of AMP on Au{100} and Au{110} surfaces and seem to be related to the gold atom density on the slab top layer. Thus, due to the high gold atom density on the Au{111} layer, there is a larger number of direct contacts between the nitrogen and oxygen atoms of AMP and the gold atoms in Au{111} in agreement with the stronger interaction predicted between AMP and the Au{111} facet. However, the number of direct atom interactions reduces in Au{100} and Au{110} with respect to Au{111} (see **Figure 7**) and this reduction explains the smaller adsorption energies in the former cases.

Finally, it must be remarked here that, according to our theoretical results, during the nanoparticle growth in presence of AMP and due to its larger affinity for the Au{111} layer, it can be expected that AMP would preferentially cover this {111} facet, deviating the deposition of gold adatoms towards less stabilized facets. This would cause the final shape of the nanoparticle to present a larger proportion of Au{111} facets, as observed in the experimental results.

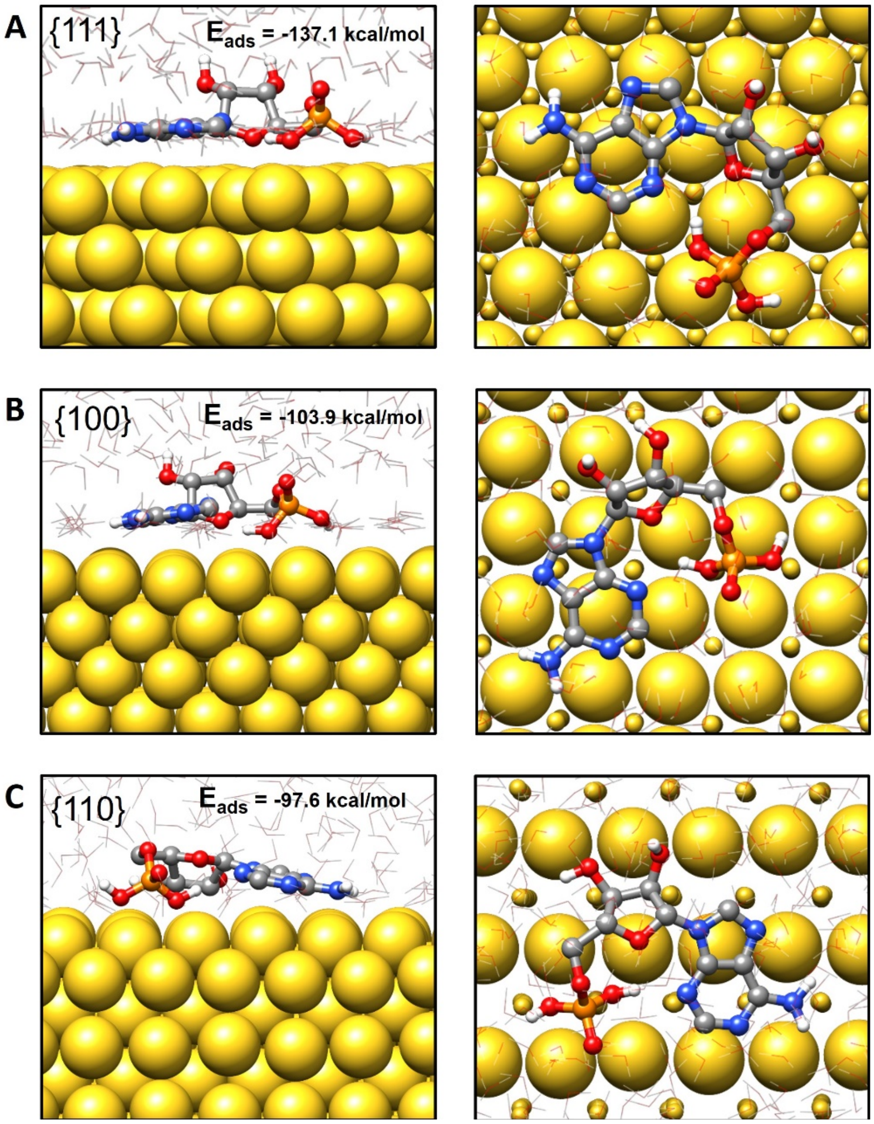

Figure 7. Side and top views of representative configurations for AMP adsorbed on (A) {111}, (B) {100} and (C) {110} Au surfaces. The adsorption energies have been included.

In summary, it seems reasonable to propose that the growth of the twin boundaries of the multi-twinned Au seeds, and therefore the formation of tips, is stimulated by the preferential adsorption of AMP molecules in [111] and [200] planes.

To further study the versatility of AMP as a capping agent, the stability of the particles in different water-miscible organic solvents was tested. **Figure 8A** shows the optical properties of the same particles when redispersed in water, ethanol, DMF and DMSO. The spectra reveal the high colloidal stability of the particles in polar organic solvents. In addition, the position of the LSPR band red-shifts upon increasing the refractive index from 1.33 to 1.36, 1.41 and 1.48, respectively. With these results, the refractive index sensitivity (RIS), defined as the shift in the LSPR band with the refractive index of the medium (Δλ/Δn), was analyzed [45] observing a good linear dependence of the LSPR with the refractive index (**Figure S14** in the SI) and RIS of 359 nm/RIU. This value aligns with other reported gold nanoparticles.[16],[46]

Next, the thermal stability of nanostars in water was also examined by heating the colloidal NP dispersion at 75 ºC or 100 ºC for one hour. As shown in **Figure 8B**, the nanostars suffer only a small blue shift in their main LSPR (*ca.* 11 and 17 nm at 75, and 100 ºC, respectively), demonstrating their good thermal stability. Note that gold nanostars have high surface energy located at the tips, where gold atoms tend to migrate towards more favourable regions, inevitably degrading their optical properties.[47]

Finally, taking into account the high stability of the particles in ethanol and the negative surface ζ-potential due to the adsorption of AMP, the silica coating was tested through the well-known Stöber method.[48] Silica coating of metal nanoparticles improves their colloidal stability, facilitates their bioconjugation, etc.[49],[50] The coating process typically requires colloids dispersed in ethanolic solution and also the presence of a capping ligand that promotes the nucleation and growth of silica on the metal surface. A range of polymers and surfactants such as polyvinylpyrrolidone (PVP)[50] or thiolated poly(ethylene glycol) (PEG)[51] have been reported for the controlled silica deposition on metal nanoparticles. Nonetheless, these approaches required a post-synthetic nanoparticles functionalization step. In the present case, we found that AMP stabilized Au nanoparticles can be directly coated with silica without any further functionalization by applying the Stöber method[48] (see Experimental section for details). **Figure 8C** shows the UV-vis-NIR spectra of two different Au nanostars before and after the silica coating. In both cases, the LSPR band red shifts upon silica coating due to the increase in the local refractive index surrounding the particles.[52] **Figure 8D** and **Figure S15** in SI show representative TEM images of the nanostars after the silica coating. All the particles are individually coated with a uniform silica shell. Both, the optical and morphological characterizations demonstrate that the spikes/tips retain their integrity, confirming the remarked ability of AMP as stabilizing agent of Au nanostars.

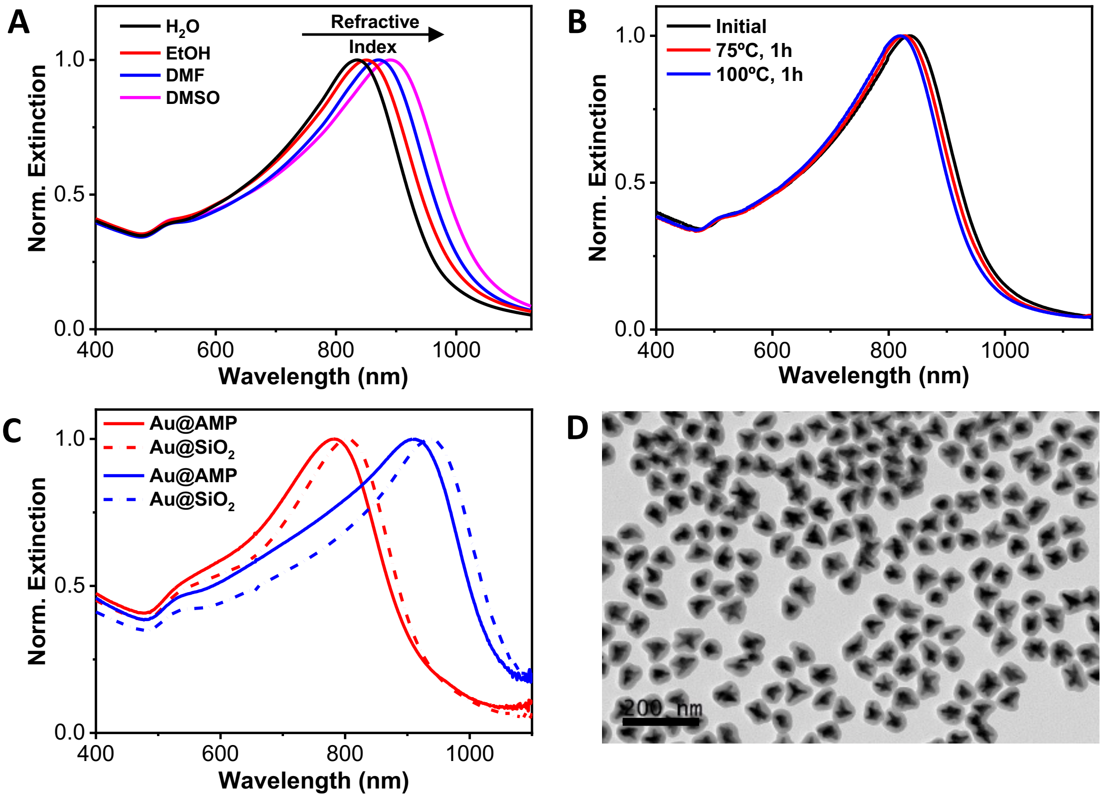

Figure 8. (A) Normalized extinction spectra of AMP-stabilized AuNSs redispersed in different solvents as indicated. (B) Normalized extinction spectra of nanostars before and after thermal treatment at 75 and 100 ºC. (C) Normalized extinction spectra of AuNSs before (solid lines) and after (dashed lines) the silica coating. (D) TEM images of silica coated AuNSs with LSPR at 750 nm.

The catalytic activity of natural peroxidases and their artificial mimics stem essentially from their unique capabilities to mediate the electron transfer from organic molecular substrates to H_2O_2. It catalyses the homolytic split of H_2O_2 to generate surface-adsorbed hydroxyls that are highly reactive toward the oxidation of the substrates. Particularly, it has been reported that gold nanoparticles can mimic the peroxidase-like activity of enzymes.[53] Furthermore, Au nanoparticles combined with certain nucleotides can improve the catalytic activity. Specifically, adenosine triphosphate (ATP) and adenosine diphosphate (ADP) were found to improve their peroxidase-like activity.[54],[55] With this idea in mind, the catalytic performance of the AuNSs was tested employing as a model reaction the oxidation of the uncoloured TMB into a blue ox-TMB in the presence of H_2O_2. AuNSs with the main LSPR at 850 nm ($AuNS_{850}$, **Figure 9A-B**) and 700 nm ($AuNS_{700}$, **Figure S16** in SI) were employed for this study. The oxidation of TMB mediated by the AuNSs was studied by UV-Vis absorption spectroscopy. As shown in **Figure 9C**, in a few seconds three absorption bands corresponding to the ox-TMB are evidenced which gradually increased in intensity with time. On the contrary, in the absence of H_2O_2 and/or gold NPs, no ox-TMB formation is detected (**Figure S16** in SI**)**. To determine the peroxidase-like performance of the AuNSs, experiments at different concentrations of TMB were carried out. **Figure 9D** shows the time evolution curves of the ox-TMB band at 652 nm observing a gradual intensity increase till reaching a plateau. Next, the initial reaction rates (V_0) were determined by taking the initial linear segment in the different curves and using a molar absorption coefficient for ox-TMB of 39.000 $M^{-1}cm^{-1}$.[56]

To fully characterize the nanoparticles as catalysts, V_0 was plotted versus TMB concentration (**Figure 9E**). The data fitted very well with the Michaelis Menten model. Finally, we estimated the constant (K_m) and maximum reaction velocity (V_{max}) using the Lineweaver Burk equation (**Equation 1** and **Figure 9F**).

$$\frac{1}{V_0} = \frac{K_m}{V_{max}\,[TMB]} + \frac{1}{V_{max}} \qquad (2)$$

Besides V_0 and V_{max} were estimated performing experiments with different concentrations of H_2O_2 (**Figures S18** and **S19** in SI).

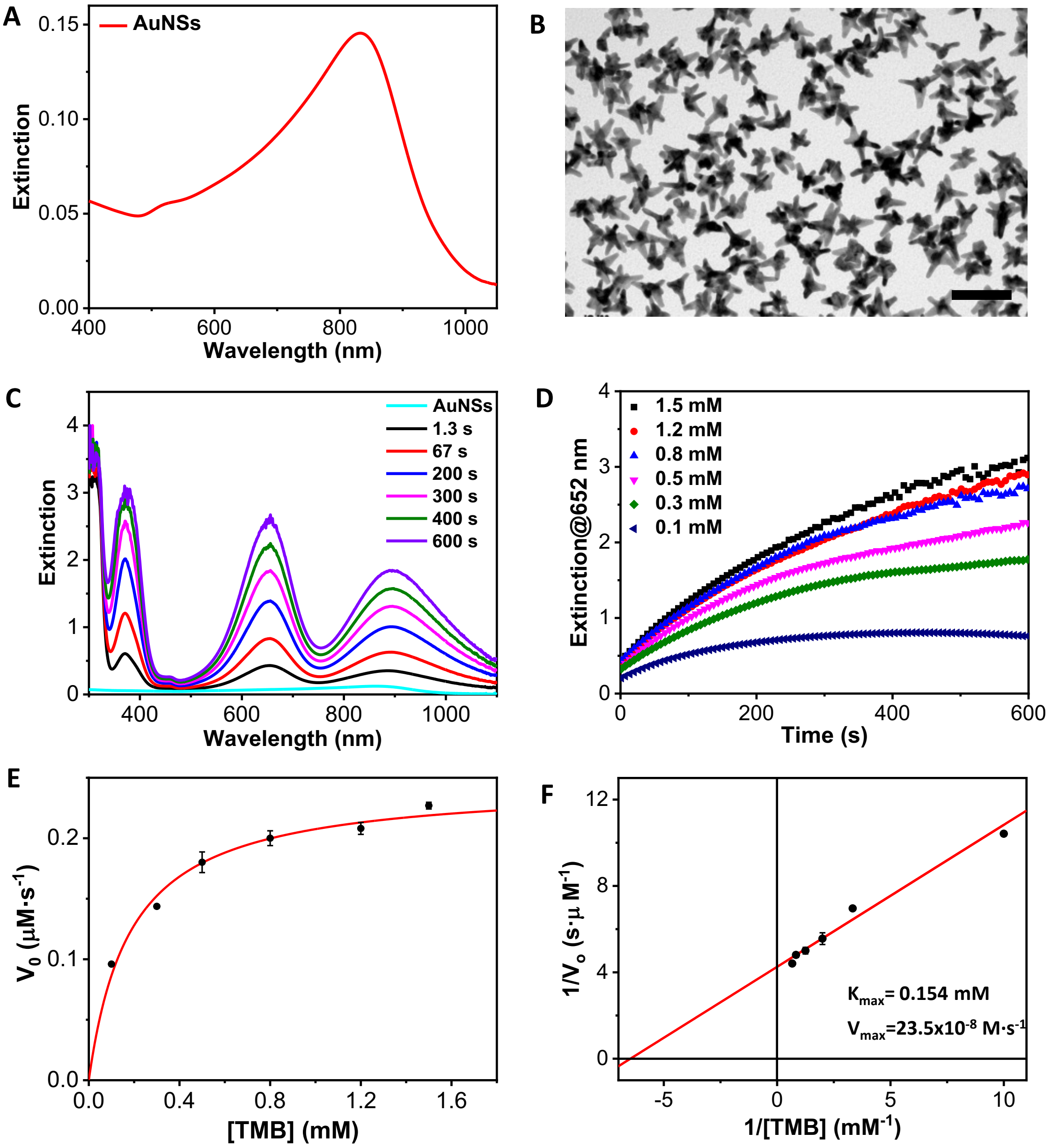

Figure 9. (A) Vis-NIR extinction spectrum and (B) TEM image of AuNSs used as catalysts. The scale bar is 100 nm. (C) Time evolution absorption spectra of the TMB oxidation in the presence of AuNSs. (D) Time evolution of the absorbance at 652 nm for different TMB concentrations, as indicated. (E) Michaelis Menten curve of AuNSs nanozymes. (F) Lineweaver Burk plot derived from the Michaelis-Menten curve. Error bars represent the standard deviation derived from three independent experiments.

For the AuNS$_{850}$, K$_m$ and V$_{max}$ values for TMB were 0.154 mM and 23.5x10^{-8} M·s^{-1}, respectively, being very similar for AuNS$_{700}$ (0.155 mM and 23.7x10^{-8} M·s^{-1}, respectively). Regarding to H_2O_2, K$_m$ and V$_{max}$ were 692.5 mM and 47.8x10^{-8} M·s^{-1}, respectively, for AuNS$_{850}$ and 721.0 mM and 49.0x10^{-8} M·s^{-1}, respectively for AuNS$_{700}$. Therefore, no significant differences were observed between both types of AuNSs. Besides, the obtained K$_m$ values

(TMB and H_2O_2) are similar to those reported in the literature for other gold nanostructures. The values of the K_m for TMB are smaller than the ones of the H_2O_2, meaning that the affinity of the nanozyme for TMB is higher.[57] Regarding the second catalytic parameter, V_{max}, the values obtained for the AuNSs were found one of the highest values reported for gold nanozymes only composed of this metal. Since, similar, or even better results can be found in the literature but using Au alloys with other metals or hybrids with organic structures such as metal-organic frameworks (MOFs) as it is summarized in **Table S2** in SI.

Conclusions

We have developed a versatile seed-mediated approach to synthesize gold nanostars in a wide size range (between 30 and 90 nm). The presence of AMP was a key point to obtain well-defined gold nanostars with tunable size and optical properties (between 580-950 nm). The number and the length of the tip, that rule out the optical properties, can be controlled through the AMP:Au molar ratio. Advanced microscopy analysis showed that the gold nanostar presents a polycrystalline nature with several tips branching out the surface. Interestingly most of the tips analyzed usually showed a twinning plane running down the tip to the core of the particle, which may indicate a preferential growth of the multitwinned crystallographic structure of the seeds used. DFT and molecular dynamics calculations support the ability of AMP as a shape-directing agent during the synthesis of the nanoparticles. Furthermore, AMP was found to be a robust capping agent since nanoparticles are colloidally stable in polar organic solvents, and also offer considerable resistance to reshaping up to 100ºC with a minimal variation in their optical response. Interestingly, we noted that the AMP provided vitriphilic properties to the manufactured AuNSs allowing their highly homogeneous silica coating, expanding the future applications of this nanomaterial. Finally, the nanostars capped with AMP displayed very good peroxidase-like catalytic properties for the TMB oxidation since the maximum reaction velocity were found among the best gold nanozymes described in literature until today.

Experimental section

Materials. Adenosine 5′-monophosphate sodium salt (AMP, ≥99%), sodium citrate tribasic dihydrate (≥98%), sodium borohydride ($NaBH_4$ ≥99), 3,3′,5,5′-Tetramethylbenzidine (TMB, ≥99%), acetic acid (100.5%), L-Ascorbic acid (≥99%), dimethyl sulfoxide (DMSO, ≥99.5), sodium hydroxide (NaOH, ≥97%), tetraethyl orthosilicate (TEOS, ≥98%) were purchased from Sigma-Aldrich. Tetrachloroaurate (III) trihydrate ($HAuCl_4 \cdot 3H_2O$, 99.99%) and Hydrogen peroxidase (H_2O_2, 35%) were supplied by Alfa Aesar. Ethanol absolute (EtOH, ≥99.9%) was purchased from Scharlau. Ammonia solution (NH_3, 35%) was purchased from Fisher Chemical. All chemicals were used as received and ultra-pure water (type I) was used in all the preparations.

Characterization. UV-Visible extinction spectra were recorded using a Cary 5000 or an Agilent 8453 spectrophotometers. Low-resolution Transmission electron microscopy (TEM) images were obtained with a JEOL JEM 1010 transmission electron microscope operating at an acceleration voltage of 100 kV. Aberration corrected Transmission Electron Microscopy was carried out using an Image and Probe-Corrected FEI Titan Themis 60-300 kV, operating at 200 kV. High angle annular dark-field scanning transmission electron microscopy (HAADF-STEM) images and electron tomography series were acquired using a Probe- Corrected FEI Titan G2 80–200 kV ChemiSTEM operating at 200 kV, with a 8 mrad convergence angle and tilt range of ±70º. ζ Potential was determined using a Zetasizer Nano S (Malvern Instruments, Malvern, UK) at 22ºC in standard 1 mL polystyrene cuvettes.

Computational methods. The initial gas phase conformational search of adenosine mono-phosphate (AMP) has been performed using the GMMX method included in the PCModel program.[58]Those conformations with relative energies below 10 kcal/mol have been further optimized employing DFT methods with the M062X functional and the 6-311+G* basis set and characterized as energy minima by computation of their harmonic vibrational frequencies using Gaussian16.

For studying the adsorption of AMP on different gold surfaces, molecular dynamic simulations were performed using GROMACS (version 2021.3)[59] with the CHARMM36 force field parameters for AMP.[60] The Lennard-Jones parameters employed for gold were those reported by Heinz et al.[61] which are designed to provide good descriptions for adsorption on different facets of metal surfaces.[62] We have employed three gold slabs representing the Au{100}, Au{110} and Au{111} surfaces with the following dimensions:

Slab	**Dimensions (Å^3)**	**Number of gold atoms**
{100}	32.6 x 32.6 x 12.2	768
{110}	32.6 x 31.7 x 11.5	704
{111}	31.7 x 30.0 x 14.1	792

As starting points for the MD simulations, we have chosen 5 different initial orientations of AMP at distances shorter than 5 Å from the surface and solvated the system with 1000 water molecules employing the TIP3P model. The size of the box was adjusted to maintain 1 g/mL density and to avoid vertical interactions, which resulted in heights for the simulation box above the surface around 3 Å. The energy of each system was minimized until the maximum force on any atom is lower than 1000 kJ mol^{-1} nm^{-1}, followed by NVT equilibration during 500 ps with a time step of 2 fs. The temperature was kept constant at 300 K employing the V-rescale thermostat and the cutoff for van-der-Waals interactions was set at 1.2 nm. Production runs were performed for 20 ns and the results for the last 10 ns were used for analysis.

To obtain the adsorption energy of AMP on each slab we employed the efficient approach of Heinz[44] which requires separated NVT simulations and energy evaluations of the solute-solvent-surface ($E_{(\mathrm{Au(slab)+AMP+H2O})}$), solute-solvent ($E_{(\mathrm{AMP+H2O})}$), solvent-surface ($E_{(\mathrm{Au(slab)+H2O})}$) and solvent ($E_{(\mathrm{H2O})}$) systems maintaining the same number of solvent molecules and altering the vertical dimension of the simulation box to keep the density close to the ideal value of 1000 kg/m^3. From these simulations, the adsorption energy is obtained as

$$E_{\mathrm{ads}} = E_{(\mathrm{Au(slab)+AMP+H2O})} - E_{(\mathrm{AMP+H2O})} + E_{(\mathrm{H2O})} - E_{(\mathrm{Au(slab)+H2O})}$$

The MD simulations for the solute-solvent system were also used for comparing the difference between isolated AMP in water and AMP adsorbed on different gold surfaces. Finally, it must be also noted that, although previous MD studies on nucleotides were performed using different unprotonated forms considering that the phosphate group is usually deprotonated in solution,[63] our molecular dynamics simulations were performed employing the completely protonated AMP. This is due to the presence of ascorbic acid as reducing agent which explains that the experimental pH of our media is around 6.5 and, according to the AMP pK_a values,[64] it is expected that most of the AMP should be present in its protonated form.

Synthesis of gold seeds (~4 nm in diameter). The synthesis of the gold seeds was based on a previous report with minor modifications.[65] 20 mL of ultra-pure water with 0.125 mM of $HAuCl_4$ and 0.25 mM of trisodium citrated were prepared into a 25 mL vial at RT. Under vigorous stirring, 250 µL of freshly prepared 10 mM $NaBH_4$ was rapidly injected. Vigorous stirring was maintained for 15 more minutes. After that, the seed solution was heated for 60 minutes at 40 ºC in an oven without agitation. Seeds can be stored at 4ºC, and they are used as it is.

Synthesis of gold seeds (~30 nm in diameter). The synthesis of the gold seeds was based on a previous method reported by Bastús et al.[66] 150 mL of an aqueous solution of 2.2 mM trisodium citrate was heated to boiling under vigorous stirring. After 15 min, 1 mL of 25 mM $HAuCl_4$ in water was injected into the boiling solution. After 10 min, the reaction mixture was cooled down to 90 °C and subsequently, another injection of 1 mL of 25 mM $HAuCl_4$ in water was performed. Another addition was repeated 30 min later. The mixture was allowed to react for 30 min and then, 55 mL were extracted from the reaction mixture. Subsequently, 53 mL of water and 2 mL of 60 mM sodium citrate (in water) were added. The resulting solution was used as Au seeds. The process was repeated four times to yield 30 nm Au NPs. To remove the excess reagents, the colloids were centrifuged twice at 2000 g for 30 min and redispersed in the same volume of water.

Synthesis of gold nanostars with ~4 nm seeds. In a 25 mL vial containing a certain volume of water (ca. 18 mL), 0.3 mL of $HAuCl_4$ (20 mM) and 0.8 mL of AMP (20 mM) were added under vigorous magnetic stirring. After 5 minutes of stirring, 0.5 mL of AA (20 mM) and 100 µL of as prepared seed solution were added. The addition of seeds must be done immediately after the addition of AA. The stirring is kept for 5 minutes and then, the vial is introduced into an oven, for 24 hours at 40 ºC without stirring. The volume of seeds was varied from 50 µL to 600 µL, and AMP concentration was varied from 0.5 mM to 0.9 mM adding the proper amount of AMP solution. To keep the final volume equal in all the experiments, the total final volume was adjusted with the volume of ultra-pure water. After the synthesis, the colloid is centrifuged twice at 3500 rpm x 30 min (5mL). The pellet of the first centrifugation was redispersed in 5 mL of NaOH 10 mM and, the pellet of the second centrifugation in 5 mL of ultra-pure water.

Synthesis of gold nanostars with ~30 nm seeds. In a 25 mL vial containing 17.4 mL of water, 0.3 mL of $HAuCl_4$ (20 mM) and 0.8 mL of AMP (20 mM) were added under vigorous magnetic stirring. After 5 minutes of stirring, 0.5 mL of AA (20 mM) and 1000 µL of as prepared seed solution were added. The addition of seeds must be immediately after the addition of AA. The stirring is kept for 5 minutes and then, the vial is introduced into an oven, for 24 hours at 40 ºC without stirring. After the synthesis, the colloid is centrifuged twice at 2000 rpm x 30 min (5mL). The pellet of the first centrifugation was redispersed in 5 mL of NaOH 10 mM and, the pellet of the second centrifugation in 5 mL of ultra-pure water.

Silica coating of gold nanostars. In a 25 mL vial containing 3.715 mL of EtOH, were added 0.5 mL of nanostars (0.5 mM Au^0) and 0.1 mL of NH_3. Under vigorous stirring, 10 µL of an ethanolic solution of 0.4 M TEOS was added. The stirring was kept for 3 hours and, finally, the colloid was centrifuged twice at 4.000 rpm for 15 min redispersing the pellet in the same volume of EtOH.

Temperature stability. In a 20 mL round bottom flask with a reflux system 10 mL of gold nanostars (0.06 mM Au^0) was added. The round bottom reaction flask was then introduced into an oil bath at 100ºC or 75ºC and stirred. After two hours, the colloid was brought to room temperature and UV-Vis absorption spectra were recorded.

Catalytic activity of nanostars nanozymes. Into a 1 cm cuvette were added 2 mL of acetate buffer solution (1.0 mM, pH = 4.0), 100 µL of nanostars (0.5 mM of Au^0) and 50 µL of TMB (32 mM in DMSO). After the homogenization of the sample, 90.5 µL of H_2O_2 (33%) was quickly added. The mixture was homogenized again and UV-Vis spectra were recorded for 600 s. All the experiments were performed at 25 ºC. To calculate the steady-state enzymatic kinetic parameters of the nanostars, various concentrations of either TMB or H_2O_2 were prepared in buffer solution always using 10 µg of nanozyme in each experiment (100 µL, 0.5 mM Au^0 of gold nanostars). For the TMB studies, TMB stock solutions of 60 mM, 48 mM, 32 mM, 20 mM, 12 mM, and 4 mM were prepared in DMSO and 50 µL of these solutions and 90.5 µL of H_2O_2 were used. In the case of study H_2O_2, 50 µL of TMB 32 mM were employed and 25, 50, 100, 200, 300, 600 µL of H_2O_2 were added. All the experiments were performed at 25 ºC.

Acknowledgments

The authors acknowledge financial support from European Innovation Council (Horizon 2020 Project: 965018 — BIOCELLPHE) the MCIN/AEI/10.13039/501100011033 (grant PID2019-108954RB-I00) and FSE ("El FSE invierte en tu futuro"), Xunta de Galicia/FEDER (grant GRC ED431C 2020/09) and the European Regional Development Fund (ERDF). The authors thank CACTI at Universidade de Vigo for TEM analysis. J.F.-L. thanks the FCT-UNL for the DL57/2016 Assistant Researcher Contract. S.N. thanks the FCT-MEC Portugal for her doctoral grant associated with the Chemistry PhD program (SFRH/BD/144618/2019). C. F.-L. acknowledges Xunta de Galicia for a predoctoral scholarship (Programa de axudas á etapa predoutoral). This work received financial support from PT national funds (FCT/MCTES, Fundação para a Ciência e Tecnologia and Ministério da Ciência, Tecnologia e Ensino Superior) through the projects UIDB/50006/2020 and UIDP/50006/2020. C.L., J.L.C., A.F.L. and S.N. thank the financial support of the Associate Laboratory Research Unit for Green Chemistry - Clean Processes and Technologies – LAQV/REQUIMTE. S. N., C. L., A. F. L., and J. F. L thanks the financial support from national funds (FCT/MCTES, Fundação para a Ciência e Tecnologia and Ministério da Ciência, Tecnologia e Ensino Superior) through project Met4cat, EXPL/QUI-COL/0263/2021. C. L., A. F. L., and J. F. L thank the financial support by the PROTEOMASS Scientific Society (Portugal) (General Funding Grants 2022-2023). This work was carried out in part through the use of the INL Advanced Electron Microscopy, Imaging and Spectroscopy Facility and Microscopy Facility at CACTI (Universidade de Vigo).

References

[1] Grzelczak, M.; Pérez-Juste, J.; Mulvaney, P.; Liz-Marzán, L. M. Shape Control in Gold Nanoparticle Synthesis. *Chem. Soc. Rev.* **2008**, *37*, 1783.

[2] Lu, C.; Zhou, S.; Gao, F.; Lin, J.; Liu, J.; Zheng, J. DNA-Mediated Growth of Noble Metal Nanomaterials for Biosensing Applications. *TrAC Trends Anal. Chem.* **2022**, *148*, 116533.

[3] Wang, Z.; Tang, L.; Tan, L. H.; Li, J.; Lu, Y. Discovery of the DNA "Genetic Code" for

Abiological Gold Nanoparticle Morphologies. *Angew. Chemie Int. Ed.* **2012**, *51*, 9078–9082.

[4] Lee, H.-E.; Ahn, H.-Y.; Mun, J.; Lee, Y. Y.; Kim, M.; Cho, N. H.; Chang, K.; Kim, W. S.; Rho, J.; Nam, K. T. Amino-Acid- and Peptide-Directed Synthesis of Chiral Plasmonic Gold Nanoparticles. *Nature* **2018**, *556*, 360–365.

[5] Ni, B.; Mychinko, M.; Gómez-Graña, S.; Morales-Vidal, J.; Obelleiro-Liz, M.; Heyvaert, W.; Vila-Liarte, D.; Zhuo, X.; Albrecht, W.; Zheng, G.; González-Rubio, G.; Taboada, J. M.; Obelleiro, F.; López, N.; Pérez-Juste, J.; Pastoriza-Santos, I.; Cölfen, H.; Bals, S.; Liz-Marzán, L. M. Chiral Seeded Growth of Gold Nanorods Into Fourfold Twisted Nanoparticles with Plasmonic Optical Activity. *Adv. Mater.* **2023**, *35*, 2208299.

[6] He, M.-Q.; Yu, Y.-L.; Wang, J.-H. Biomolecule-Tailored Assembly and Morphology of Gold Nanoparticles for LSPR Applications. *Nano Today* **2020**, *35*, 101005.

[7] Reguera, J.; Langer, J.; Jiménez de Aberasturi, D.; Liz-Marzán, L. M. Anisotropic Metal Nanoparticles for Surface Enhanced Raman Scattering. *Chem. Soc. Rev.* **2017**, *46*, 3866–3885.

[8] Becerril-Castro, I. B.; Calderon, I.; Pazos-Perez, N.; Guerrini, L.; Schulz, F.; Feliu, N.; Chakraborty, I.; Giannini, V.; Parak, W. J.; Alvarez-Puebla, R. A. Gold Nanostars: Synthesis, Optical and SERS Analytical Properties. *Anal. Sens.* **2022**, *2*.

[9] Tavakkoli Yaraki, M.; Wu, M.; Middha, E.; Wu, W.; Daqiqeh Rezaei, S.; Liu, B.; Tan, Y. N. Gold Nanostars-AIE Theranostic Nanodots with Enhanced Fluorescence and Photosensitization Towards Effective Image-Guided Photodynamic Therapy. *Nano-Micro Lett.* **2021**, *13*, 58.

[10] Kang, Z.; Liu, M.; Li, Z.; Li, S.; Jia, Z.; Liu, C.; Qin, W.; Qin, G. Passively Q-Switched Erbium Doped Fiber Laser Using a Gold Nanostars Based Saturable Absorber. *Photonics Res.* **2018**, *6*, 549.

[11] Espinosa, A.; Silva, A. K. A.; Sánchez-Iglesias, A.; Grzelczak, M.; Péchoux, C.; Desboeufs, K.; Liz-Marzán, L. M.; Wilhelm, C. Cancer Cell Internalization of Gold Nanostars Impacts Their Photothermal Efficiency In Vitro and In Vivo: Toward a Plasmonic Thermal Fingerprint in Tumoral Environment. *Adv. Healthc. Mater.* **2016**, *5*, 1040–1048.

[12] Priecel, P.; Adekunle Salami, H.; Padilla, R. H.; Zhong, Z.; Lopez-Sanchez, J. A. Anisotropic Gold Nanoparticles: Preparation and Applications in Catalysis. *Chinese J. Catal.* **2016**, *37*, 1619–1650.

[13] Barbosa, S.; Agrawal, A.; Rodríguez-Lorenzo, L.; Pastoriza-Santos, I.; Alvarez-Puebla, R. A.; Kornowski, A.; Weller, H.; Liz-Marzán, L. M. Tuning Size and Sensing Properties in Colloidal Gold Nanostars. *Langmuir* **2010**, *26*, 14943–14950.

[14] Khoury, C. G.; Vo-Dinh, T. Gold Nanostars For Surface-Enhanced Raman Scattering: Synthesis, Characterization and Optimization. *J. Phys. Chem. C* **2008**, *112*, 18849–18859.

[15] Jana, D.; Matti, C.; He, J.; Sagle, L. Capping Agent-Free Gold Nanostars Show Greatly Increased Versatility and Sensitivity for Biosensing. *Anal. Chem.* **2015**, *87*, 3964–3972.

[16] Nuti, S.; Fernández-Lodeiro, C.; Fernández-Lodeiro, J.; Fernández-Lodeiro, A.; Pérez-Juste, J.; Pastoriza-Santos, I.; LaGrow, A. P.; Schraidt, O.; Luis Capelo-Martínez, J.; Lodeiro, C. Polyallylamine Assisted Synthesis of 3D Branched AuNPs with Plasmon Tunability in the Vis-NIR Region as Refractive Index Sensitivity Probes. *J. Colloid Interface Sci.* **2022**, *611*, 695–705.

[17] Kariuki, V. M.; Hoffmeier, J. C.; Yazgan, I.; Sadik, O. A. Seedless Synthesis and SERS Characterization of Multi-Branched Gold Nanoflowers Using Water Soluble Polymers. *Nanoscale* **2017**, *9*, 8330–8340.

[18] Djafari, J.; Fernández-Lodeiro, A.; García-Lojo, D.; Fernández-Lodeiro, J.; Rodríguez-González, B.; Pastoriza-Santos, I.; Pérez-Juste, J.; Capelo, J. L.; Lodeiro, C. Iron(II) as a Green Reducing Agent in Gold Nanoparticle Synthesis. *ACS Sustain. Chem. Eng.* **2019**, *7*, 8295–8302.

[19] Liebig, F.; Henning, R.; Sarhan, R. M.; Prietzel, C.; Schmitt, C. N. Z.; Bargheer, M.; Koetz, J. A Simple One-Step Procedure to Synthesise Gold Nanostars in Concentrated Aqueous Surfactant Solutions. *RSC Adv.* **2019**, *9*, 23633–23641.

[20] Sau, T. K.; Murphy, C. J. Room Temperature, High-Yield Synthesis of Multiple Shapes of Gold Nanoparticles in Aqueous Solution. *J. Am. Chem. Soc.* **2004**, *126*, 8648–8649.

[21] Blanch, A. J.; Döblinger, M.; Rodríguez-Fernández, J. Simple and Rapid High-Yield Synthesis and Size Sorting of Multibranched Hollow Gold Nanoparticles with Highly Tunable NIR Plasmon Resonances (Small 35/2015). *Small* **2015**, *11*, 4549–4549.

[22] Kuo, C.-H.; Huang, M. H. Synthesis of Branched Gold Nanocrystals by a Seeding Growth Approach. *Langmuir* **2005**, *21*, 2012–2016.

[23] Pallavicini, P.; Chirico, G.; Collini, M.; Dacarro, G.; Donà, A.; D'Alfonso, L.; Falqui, A.; Diaz-Fernandez, Y.; Freddi, S.; Garofalo, B.; Genovese, A.; Sironi, L.; Taglietti, A. Synthesis of Branched Au Nanoparticles with Tunable Near-Infrared LSPR Using a Zwitterionic Surfactant. *Chem. Commun.* **2011**, *47*, 1315–1317.

[24] Webb, J. A.; Erwin, W. R.; Zarick, H. F.; Aufrecht, J.; Manning, H. W.; Lang, M. J.; Pint, C. L.; Bardhan, R. Geometry-Dependent Plasmonic Tunability and Photothermal Characteristics of Multibranched Gold Nanoantennas. *J. Phys. Chem. C* **2014**, *118*, 3696–3707.

[25] Maiorano, G.; Rizzello, L.; Malvindi, M. A.; Shankar, S. S.; Martiradonna, L.; Falqui, A.; Cingolani, R.; Pompa, P. P. Monodispersed and Size-Controlled Multibranched Gold Nanoparticles with Nanoscale Tuning of Surface Morphology. *Nanoscale* **2011**, *3*, 2227.

[26] M. Pallares, R.; Stilson, T.; Choo, P.; Hu, J.; Odom, T. W. Using Good's Buffers To Control the Anisotropic Structure and Optical Properties of Spiky Gold Nanoparticles for Refractive Index Sensing. *ACS Appl. Nano Mater.* **2019**, *2*, 5266–5271.

[27] Chandra, K.; Culver, K. S. B.; Werner, S. E.; Lee, R. C.; Odom, T. W. Manipulating the Anisotropic Structure of Gold Nanostars Using Good's Buffers. *Chem. Mater.* **2016**, *28*, 6763–

6769.

[28] Xie, J.; Lee, J. Y.; Wang, D. I. C. Seedless, Surfactantless, High-Yield Synthesis of Branched Gold Nanocrystals in HEPES Buffer Solution. *Chem. Mater.* **2007**, *19*, 2823–2830.

[29] Li, J.; Cai, R.; Kawazoe, N.; Chen, G. Facile Preparation of Albumin-Stabilized Gold Nanostars for the Targeted Photothermal Ablation of Cancer Cells. *J. Mater. Chem. B* **2015**, *3*, 5806–5814.

[30] Lu, L.; Ai, K.; Ozaki, Y. Environmentally Friendly Synthesis of Highly Monodisperse Biocompatible Gold Nanoparticles with Urchin-like Shape. *Langmuir* **2008**, *24*, 1058–1063.

[31] Sajitha, M.; Vindhyasarumi, A.; Gopi, A.; Yoosaf, K. Shape Controlled Synthesis of Multi-Branched Gold Nanocrystals through a Facile One-Pot Bifunctional Biomolecular Approach. *RSC Adv.* **2015**, *5*, 98318–98324.

[32] Bian, P.; Yuan, J.; Han, H.; Ma, Z. A Seedless, Surfactant-Free Synthesis of Gold Nanospheres, Nanosheets, and Nanostars Based on Functionalized Tryptophan. *J. Nanosci. Nanotechnol.* **2016**, *16*, 7503–7508.

[33] Green, M.; Smyth-Boyle, D. Directed Growth of Gold Nanostructures Using a Nucleoside/Nucleotide. *J. Mater. Chem.* **2007**, *17*, 3588.

[34] Ungor, D.; Csapó, E.; Kismárton, B.; Juhász, Á.; Dékány, I. Nucleotide-Directed Syntheses of Gold Nanohybrid Systems with Structure-Dependent Optical Features: Selective Fluorescence Sensing of Fe3+ Ions. *Colloids Surfaces B Biointerfaces* **2017**, *155*, 135–141.

[35] Zhao, W.; Gonzaga, F.; Li, Y.; Brook, M. A. Highly Stabilized Nucleotide-Capped Small Gold Nanoparticles with Tunable Size. *Adv. Mater.* **2007**, *19*, 1766–1771.

[36] Huang, P.; Pandoli, O.; Wang, X.; Wang, Z.; Li, Z.; Zhang, C.; Chen, F.; Lin, J.; Cui, D.; Chen, X. Chiral Guanosine 5′-Monophosphate-Capped Gold Nanoflowers: Controllable Synthesis, Characterization, Surface-Enhanced Raman Scattering Activity, Cellular Imaging and Photothermal Therapy. *Nano Res.* **2012**, *5*, 630–639.

[37] Pu, F.; Ren, J.; Qu, X. Nucleobases, Nucleosides, and Nucleotides: Versatile Biomolecules for Generating Functional Nanomaterials. *Chem. Soc. Rev.* **2018**, *47*, 1285–1306.

[38] Kundu, J.; Neumann, O.; Janesko, B. G.; Zhang, D.; Lal, S.; Barhoumi, A.; Scuseria, G. E.; Halas, N. J. Adenine− and Adenosine Monophosphate (AMP)−Gold Binding Interactions Studied by Surface-Enhanced Raman and Infrared Spectroscopies. *J. Phys. Chem. C* **2009**, *113*, 14390–14397.

[39] Berti, L.; Burley, G. A. Nucleic Acid and Nucleotide-Mediated Synthesis of Inorganic Nanoparticles. *Nat. Nanotechnol.* **2008**, *3*, 81–87.

[40] He, Y.; Zhou, L. A Theoretical Study on Pyridine Gold (III) Complexes AuCl 3 (Hpm) and AuCl 2 (Pm) Targeting Purine Bases and Cysteine. *Comput. Theor. Chem.* **2016**, *1093*, 20–28.

[41] Jana, N. R.; Gearheart, L.; Murphy, C. J. Evidence for Seed-Mediated Nucleation in the Chemical Reduction of Gold Salts to Gold Nanoparticles. *Chem. Mater.* **2001**, *13*, 2313–2322.

[42] Senthil Kumar, P.; Pastoriza-Santos, I.; Rodríguez-González, B.; Javier García de Abajo, F.; Liz-Marzán, L. M. High-Yield Synthesis and Optical Response of Gold Nanostars. *Nanotechnology* **2008**, *19*, 015606.

[43] Barbosa, S.; Agrawal, A.; Rodríguez-Lorenzo, L.; Pastoriza-Santos, I.; Alvarez-Puebla, R. A.; Kornowski, A.; Weller, H.; Liz-Marzán, L. M. Tuning Size and Sensing Properties in Colloidal Gold Nanostars. *Langmuir* **2010**, *26*, 14943–14950.

[44] Heinz, H. Computational Screening of Biomolecular Adsorption and Self-Assembly on Nanoscale Surfaces. *J. Comput. Chem.* **2009**, NA-NA.

[45] Sepúlveda, B.; Angelomé, P. C.; Lechuga, L. M.; Liz-Marzán, L. M. LSPR-Based Nanobiosensors. *Nano Today* **2009**, *4*, 244–251.

[46] Rodal-Cedeira, S.; Montes-García, V.; Polavarapu, L.; Solís, D. M.; Heidari, H.; La Porta, A.; Angiola, M.; Martucci, A.; Taboada, J. M.; Obelleiro, F.; Bals, S.; Pérez-Juste, J.; Pastoriza-Santos, I. Plasmonic Au@Pd Nanorods with Boosted Refractive Index Susceptibility and SERS Efficiency: A Multifunctional Platform for Hydrogen Sensing and Monitoring of Catalytic Reactions. *Chem. Mater.* **2016**, *28*, 9169–9180.

[47] Fabris, L. Gold Nanostars in Biology and Medicine: Understanding Physicochemical Properties to Broaden Applicability. *J. Phys. Chem. C* **2020**, *124*, 26540–26553.

[48] Stöber, W.; Fink, A.; Bohn, E. Controlled Growth of Monodisperse Silica Spheres in the Micron Size Range. *J. Colloid Interface Sci.* **1968**, *26*, 62–69.

[49] Kang, H.; Buchman, J. T.; Rodriguez, R. S.; Ring, H. L.; He, J.; Bantz, K. C.; Haynes, C. L. Stabilization of Silver and Gold Nanoparticles: Preservation and Improvement of Plasmonic Functionalities. *Chem. Rev.* **2019**, *119*, 664–699.

[50] Guerrero-Martínez, A.; Pérez-Juste, J.; Liz-Marzán, L. M. Recent Progress on Silica Coating of Nanoparticles and Related Nanomaterials. *Adv. Mater.* **2010**, *22*, 1182–1195.

[51] Fales, A. M.; Yuan, H.; Vo-Dinh, T. Silica-Coated Gold Nanostars for Combined Surface-Enhanced Raman Scattering (SERS) Detection and Singlet-Oxygen Generation: A Potential Nanoplatform for Theranostics. *Langmuir* **2011**, *27*, 12186–12190.

[52] Liz-Marzán, L. M.; Giersig, M.; Mulvaney, P. Synthesis of Nanosized Gold−Silica Core−Shell Particles. *Langmuir* **1996**, *12*, 4329–4335.

[53] Ji, X.; Li, Q.; Su, R.; Wang, Y.; Qi, W. Peroxidase-Mimicking Hierarchically Organized Gold Particles for Glucose Detection. *Langmuir* **2023**, *39*, 3216–3224.

[54] Shah, J.; Singh, S. Unveiling the Role of ATP in Amplification of Intrinsic Peroxidase-like Activity of Gold Nanoparticles. *3 Biotech* **2018**, *8*, 67.

[55] Shah, J.; Purohit, R.; Singh, R.; Karakoti, A. S.; Singh, S. ATP-Enhanced Peroxidase-like Activity of Gold Nanoparticles. *J. Colloid Interface Sci.* **2015**, *456*, 100–107.

[56] Josephy, P. D.; Eling, T.; Mason, R. P. The Horseradish Peroxidase-Catalyzed Oxidation of 3,5,3’,5’-Tetramethylbenzidine. Free Radical and Charge-Transfer Complex Intermediates. *J.*

Biol. Chem. **1982**, *257*, 3669–3675.

[57] Ma, M.; Cao, J.; Fang, A.; Xu, Z.; Zhang, T.; Shi, F. Detection and Difference Analysis of the Enzyme Activity of Colloidal Gold Nanoparticles With Negatively Charged Surfaces Prepared by Different Reducing Agents. *Front. Chem.* **2022**, *9*.

[58] Gille, A. L.; Dutmer, B. C.; Gilbert, T. M. PCMODEL 9.2. *J. Am. Chem. Soc.* **2009**, *131*, 5714–5714.

[59] Abraham, M. J.; Murtola, T.; Schulz, R.; Páll, S.; Smith, J. C.; Hess, B.; Lindahl, E. GROMACS: High Performance Molecular Simulations through Multi-Level Parallelism from Laptops to Supercomputers. *SoftwareX* **2015**, *1–2*, 19–25.

[60] Vanommeslaeghe, K.; Hatcher, E.; Acharya, C.; Kundu, S.; Zhong, S.; Shim, J.; Darian, E.; Guvench, O.; Lopes, P.; Vorobyov, I.; Mackerell, A. D. CHARMM General Force Field: A Force Field for Drug-like Molecules Compatible with the CHARMM All-Atom Additive Biological Force Fields. *J. Comput. Chem.* **2009**, NA-NA.

[61] Heinz, H.; Vaia, R. A.; Farmer, B. L.; Naik, R. R. Accurate Simulation of Surfaces and Interfaces of Face-Centered Cubic Metals Using 12−6 and 9−6 Lennard-Jones Potentials. *J. Phys. Chem. C* **2008**, *112*, 17281–17290.

[62] Ramezani-Dakhel, H.; Ruan, L.; Huang, Y.; Heinz, H. Molecular Mechanism of Specific Recognition of Cubic Pt Nanocrystals by Peptides and of the Concentration-Dependent Formation from Seed Crystals. *Adv. Funct. Mater.* **2015**, *25*, 1374–1384.

[63] Gruszczyński, P.; Smalara, K.; Obuchowski, M.; Kaźmierkiewicz, R. ATP and Its N6-Substituted Analogues: Parameterization, Molecular Dynamics Simulation and Conformational Analysis. *J. Mol. Model.* **2011**, *17*, 1081–1090.

[64] Alberty, R.; Smith, R.; Bock, R. THE APPARENT IONIZATION CONSTANTS OF THE ADENOSINEPHOSPHATES AND RELATED COMPOUNDS. *J. Biol. Chem.* **1951**, *193*, 425–434.

[65] Pérez-Juste, J.; Liz-Marzán, L. M.; Carnie, S.; Chan, D. Y. C.; Mulvaney, P. Electric-Field-Directed Growth of Gold Nanorods in Aqueous Surfactant Solutions. *Adv. Funct. Mater.* **2004**, *14*, 571–579.

[66] Bastús, N. G.; Comenge, J.; Puntes, V. Kinetically Controlled Seeded Growth Synthesis of Citrate-Stabilized Gold Nanoparticles of up to 200 Nm: Size Focusing versus Ostwald Ripening. *Langmuir* **2011**, *27*, 11098–11105.